# MEASUREMENT OF THERMAL PROCESSING VARIABILITY IN POWDER BED FUSION

**Jarred C. Heigel[1], Eric Whitenton[1]**
**[1]Engineering Laboratory**
**National Institute of Standards and Technology[2]**
**Gaithersburg, MD, USA**

## INTRODUCTION

Laser powder bed fusion (LPBF) is an additive manufacturing (AM) technology used to manufacture high-value metal parts. The layer-by-layer nature of the process allows complex geometries and internal features, such as conformal cooling channels, to be realized. For the technology to reach its full potential, it must be capable of manufacturing precision parts. However, the precision of parts fabricated using LPBF is currently orders of magnitude worse than what can be achieved using machining [1]. This is due, in part, to the distortion that arises from thermally induced residual stresses [2]. While distortion can be compensated for and/or corrected through post-processing, this is costly and not always possible for internal features.

An additional challenge that LPBF and other metal AM technologies face is that in addition to creating the part geometry, the material is also created during the process. The melting of the metal feedstock powder using a laser and the rapid cooling of the solidified material, as well as the cyclic re-heating and cooling from adjacent tracks and subsequent layers, has a significant impact on microstructure and material properties [3]. Unfortunately, the material of a LPBF manufactured part is inhomogeneous due to the inconsistency of the thermal processing throughout the part. The imprecision arises from a variety of factors, including the scan strategy, processing conditions [4], and geometric effects, such as the reduced ability to conduct heat away from the melt pool when creating overhangs.

Considering the impact on distortion, microstructure, and material performance, the thermal history of the processed material must be understood before precision geometries or materials can be manufactured using LPBF technologies. The objective of this work is to present preliminary results from in situ thermographic measurements acquired during the build of a complex part and to assess the variability of the thermal processing in response to scan strategy and geometry effects.

## EXPERIMENT SETUP

FIGURE 1 shows the experiment setup. A commercial powder bed fusion system is modified to allow a high-speed short-wave infrared (SWIR) camera to observe a small region of the build plane. The camera acquires images at a rate of 1800 frames per second and is sensitive to radiant temperatures from 550 °C to 1050 °C. Details on this setup can be found in [5].

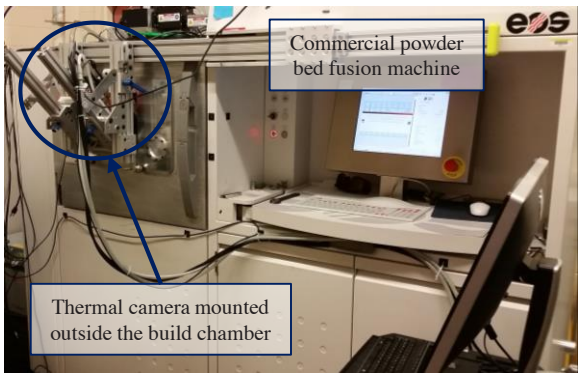


*FIGURE 1 - The powder bed fusion system with the infrared camera mounted to it.*

[2] Official contribution of the National Institute of Standards and Technology (NIST); not subject to copyright in the USA. The full descriptions of the procedures used in this paper require the identification of certain commercial products. The inclusion of such information should in no way be construed as indicating that such products are endorsed by NIST or are recommended by NIST or that they are necessarily the best materials, instruments, software, or suppliers for the purposes described.

FIGURE 2 shows the part used in this study, manufactured of nickel-based super alloy 625 (IN 625). FIGURE 3 presents a schematic of the part. The part is designed to be small enough to fit entirely in the field of view of the camera, which is approximately 12 mm x 6 mm. It has a hole on one side and a 45° overhang on the other. The part is manufactured on a 100 mm x 50 mm IN 625 substrate that is 12.7 mm thick. The substrate is bolted on the LPBF build platform.

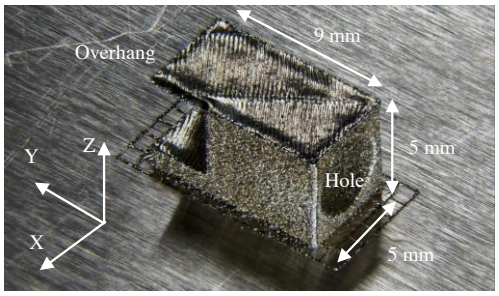


*FIGURE 2 - The part used in this study is small enough to fit in the SWIR camera's field of view.*

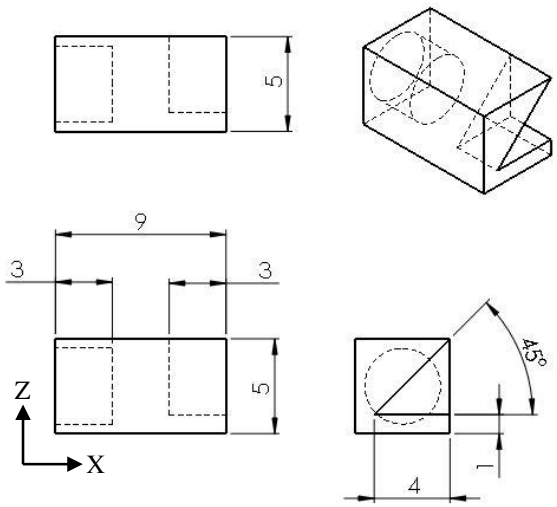


*FIGURE 3 – Part schematic. Dimensions in* mm.

The part is manufactured in 249 layers. Each layer is 20 μm thick and consists of three steps: a pre-contour scan of the perimeter of the part, a raster scan to fill in the cross section of the part (called "skin" by the manufacturer), and a post-contour scan of the perimeter. This study focuses on the thermal history generated by the raster scan. The raster scan is performed with a programmed laser power of 195 W and a programmed scan speed of 800 mm/s. The hatch spacing (distance between adjacent scan tracks) is 0.1 mm. The raster scans are contained within "stripes" that are 5 mm wide. These stripes are pre-defined within the build area and rotate 67° between layers. Multiple stripes are used in each layer to scan the entire cross section of the part.

There are four layers of interest due to the part geometry, as shown in FIGURE 4. Layer 25 is the final layer of the 9 mm long 5 mm wide rectangular base. It provides insight into the thermal history unaffected by the hole or overhang features and establishes a baseline to which the other layers can be compared. Layer 125 occurs at the midpoint of the hole where the width of the wall beside it is at a minimum (0.5 mm thick). Layer 226 is performed immediately after the hole is completed and therefore part of the layer is created over powder and not solidified material. Finally, Layer 249 is the final layer, the effects of which are evident in the top of the part (FIGURE 2).

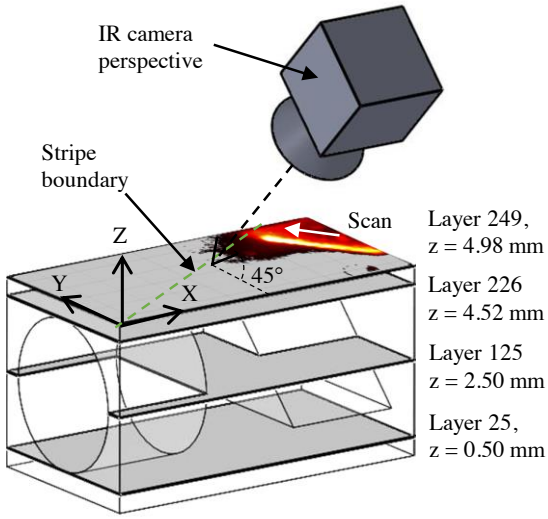


*FIGURE 4 - Illustration of the 4 layers of interest and the relative position of the IR camera.*

**RESULTS AND DISCUSSION**

An example thermal video frame acquired during Layer 25 is show in FIGURE 5. This is one of the 1266 frames acquired during the layer. In this frame (# 617), the laser is scanning through the middle of the part in a 5 mm-wide stripe. The stripe boundary is illustrated with dashed green lines. Ejected material (spatter) is imaged in addition to the melt pool.

FIGURE 6A illustrates the radiant temperature history of a single pixel during the processing of

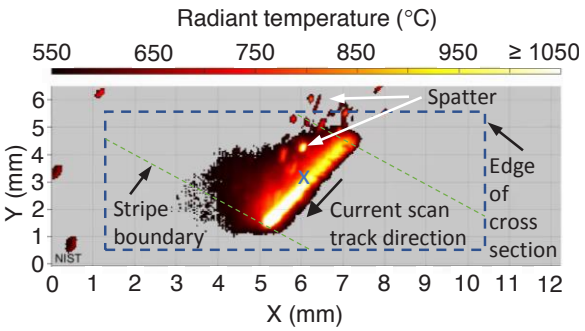


*FIGURE 5 - A thermal video frame acquired during Layer 25. The part perimeter is illustrated with the dashed lines. The blue "x" in the center shows the location of the data in FIGURE 6.*

Layer 25. This pixel correlates to the location indicated by a blue "x" in FIGURE 5. As expected, the measured radiant temperature fluctuates as the material is re-heated, and (in some cases) re-melted by successive tracks. The oscillation continues as the material cools. Spatter flying between the surface and the camera causes extreme spikes.

FIGURE 6B demonstrates the calculation of the cooling rate for each pixel in a layer. For this study, cooling rate is defined as the rate the material cools from the true temperature of solidification of 1290 °C to 1000 °C. Since the SWIR camera measures radiant temperature and not true temperature, the equivalent radiant temperatures must be determined.

The radiant temperature equivalent to the solidification temperature was identified in prior work [5]. Using the same experiment setup, the solidification plateau was identified and used to measure melt pool length and to identify the solidification radiant temperature when creating laser tracks on bare substrates [5]. A subsequent study demonstrated that the presence of powder does not significantly affect the radiant temperature [7]. Therefore, radiant temperature of solidification determined from bare plate scans (942 °C) is assumed for the multi-layer build.

The radiant and true temperatures of solidification can be used to calculate the effective emissivity using the Sakuma-Hatori equations, which relate the camera signal to a calibrated temperature [8]:

$$F(T) = S = \frac{C}{exp\left(\frac{c_2}{AT+B}\right)-1} \quad (1)$$

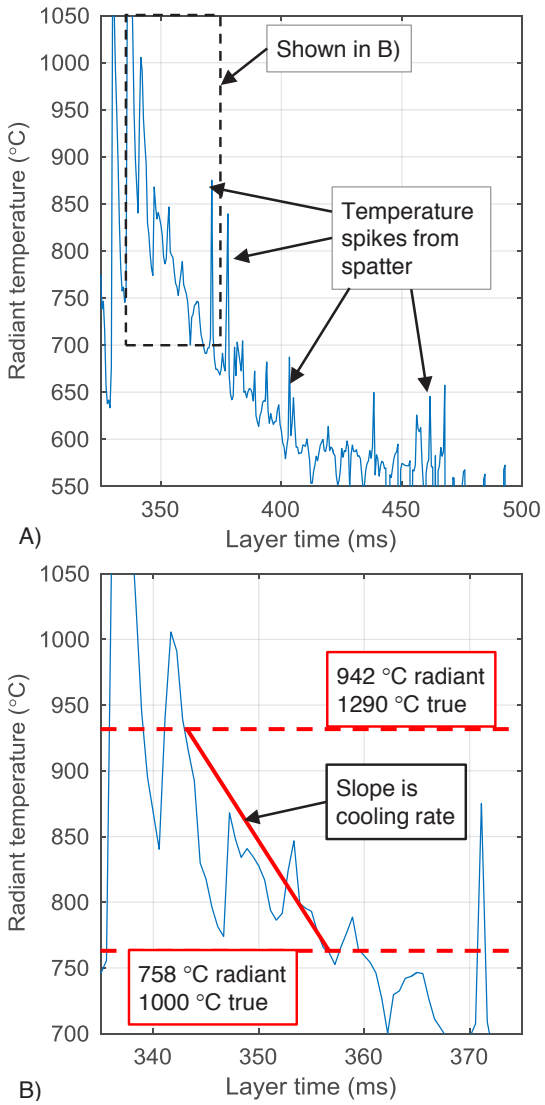


*FIGURE 6 - Radiant temperature history at the center of the part in Layer 25.*

$$F^{-1}(S) = T_{radiant} = \frac{c_2}{A\,ln\left(\frac{C}{S}+1\right)} - \frac{B}{A} \quad (2)$$

where *S* is the camera signal, *T* is temperature in K, $c_2$ is the second radiation constant (14388 μm·K) and *A*, *B*, and *C* are constants established through a black body calibration. The black body calibration and the resulting constants for this work are presented in [5]. True temperature and radiant temperature are related:

$$F(T_{true})\,\varepsilon = F(T_{radiant}) \quad (3)$$

where ε is the effective emissivity of the surface. The effective emissivity of the recently solidified material is calculated using Equation 3 and the true and radiant temperatures of the solidification. This calculation yields $\varepsilon = 0.168$. Assuming this

emissivity applies to the material at 1000 °C, the equivalent radiant temperature is 758 °C. Cooling rate is then calculated using:

$$Cooling\ Rate = \frac{\Delta T_{true}}{t_2 - t_1} \quad (4)$$

where $\Delta T_{true}$ is the temperature range of interest (in this case, 290 °C), $t_1$ is the time at that occurrence the pixel drops below the solidification temperature, and $t_2$ is first time after $t_1$ that the pixel equals the lower temperature range.

FIGURE 7 presents a map of the cooling rate calculated from the SWIR measurements of Layer 25. This figure shows that cooling rate varies significantly due to both scan strategy and layer shape. The typical behavior within a stripe unaffected by the layer shape is evident in the center region of the layer (outlined with white dashes). The cooling rate is lower in the center of the stripe (approximately 25 000 °C/s) and higher near the edges (more than 50 000 °C/s). This difference is attributed to the material in the middle of the stripe retaining heat longer than at the edges of the strip, decreasing its ability to evacuate the heat input from the laser and thus decreasing the rate at which the material cools. While this trend is expected to be consistent for different stripe widths (a variable that most LPBF users can control), the magnitudes may differ.

Although a typical cooling rate distribution within a stripe can be achieved, the layer shape can significantly alter the scan strategy and ultimately the cooling rates. For instance, the shape of Layer 25 prevents most of the area from being scanned with the programmed stripe width. The stripe width is effectively decreased to scan these narrower areas, and the laser more frequently re-scans near a recently solidified region, thus keeping the material hotter and reducing the material's ability to evacuate heat input from the laser. Additionally, the timing of the laser seems to be affected when the geometry decreases the stripe width [6], slightly increasing the time between the end of one scan track and the beginning of the next. These two factors explain the lower cooling rates in the 1st and 3rd stripes that fill the upper right and lower left corners of the layer, and the beginning and end of the 2nd stripe across the center of the layer.

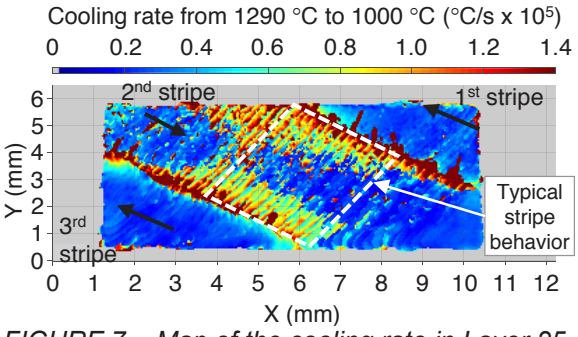


*FIGURE 7 – Map of the cooling rate in Layer 25.*

Histograms are used to assess the cooling rate as a percentage of area within a layer or region of interest. FIGURE 8 compares the typical stripe (region in FIGURE 7), Layer 25, and all layers from 1 through 25 (considered a baseline for analysis of the rest of the layers). Three observations are made from these histograms. First, within a typical stripe (in this build), two distinct cooling rates occur, where the edges of the stripe cool more approximately 3 times faster than the center of the stripe. Second, the effective decreasing of the stripe width to complete a layer increases the occurrence of lower cooling rate (comparing Layer 25 to the typical stripe). Third, Layer 25 is representative of the baseline established using all preceding layers, (similarity between the two histograms).

FIGURE 9 shows the cooling rate calculations and analysis of Layer 125, which demonstrates the impact of the narrow features on either side of the hole. The analysis reveals that the cooling rate in the narrow features increases by a factor of 2 to approximately 50 000 °C/s, whereas the cooling rate in the rest of the layer remains comparable to the baseline. These results are

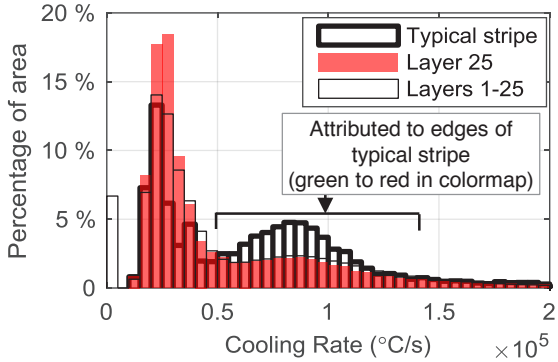


*FIGURE 8 - Histogram showing cooling rate as a function of area within the layer.*

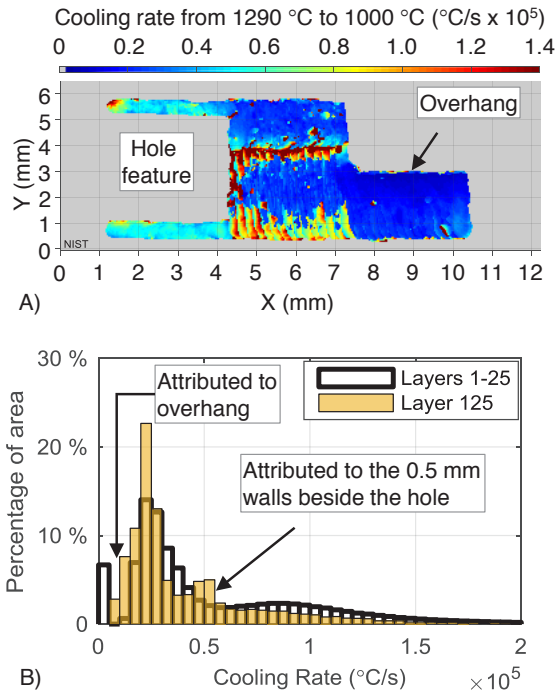


*FIGURE 9 - Cooling rate measured during Layer 125. A) Measured cooling rate at each pixel in the layer, B) comparison with Layers 1 through 25.*

counter-intuitive for two reasons. First, the narrow scans are performed on material that is surrounded by a greater percentage of powder, which is insulative, compared to the bulk. The higher thermal resistance would theoretically lead to slower cooling rates. Second, the stripe width in these features is much narrower than typical. It has been demonstrated earlier that this decreases cooling rate. However, the increased cooling rate in these narrow features may result from the ratio between laser-on and laser-off times decreasing. The laser shutter is open for a very short duration to scan the 0.5 mm wide features, while the time between successive laser tracks is not significantly impacted. Furthermore, the time to scan each of the narrow features is very quick, potentially impacting of material pre-heating which can decrease conductivity. Further experimental and modeling efforts are required confirm these hypotheses.

FIGURE 10 presents the cooling rate in Layer 226 and compares the results to the baseline. This layer occurs immediately after the completion of the hole feature. FIGURE 10A shows that while a portion of the stripe above the hole experiences cooling rates slower than expected in a typical stripe, a small portion directly above the top of the hole experiences a higher cooling rate. The lower cooling rate is caused by the geometry, since there is less solid mass below the layer to conduct heat away, while the small region with a higher cooling rate is a result of the scan strategy, as explained below.

The thermal video of Layer 226 shows that most of the stripe is executed as expected, but the laser skips over a small area directly above the hole. After all the stripes are completed, the laser then scans the area that was skipped over. This scan after the completion of all the stripes is referred to by the manufacturer as a “down-skin” and is used for material with powder directly underneath the layer. The “down-skin” is performed with process parameters that produce a shallower melt pool, minimizing the chance of over-melting. Although these “down-skin” scans are performed with little or no solid material underneath, the cooling rate is faster for two reasons. First, the altered processing parameters used for these scans results in lower energy and less heating of the part. Second, the surrounding material to the sides of this regions is better able

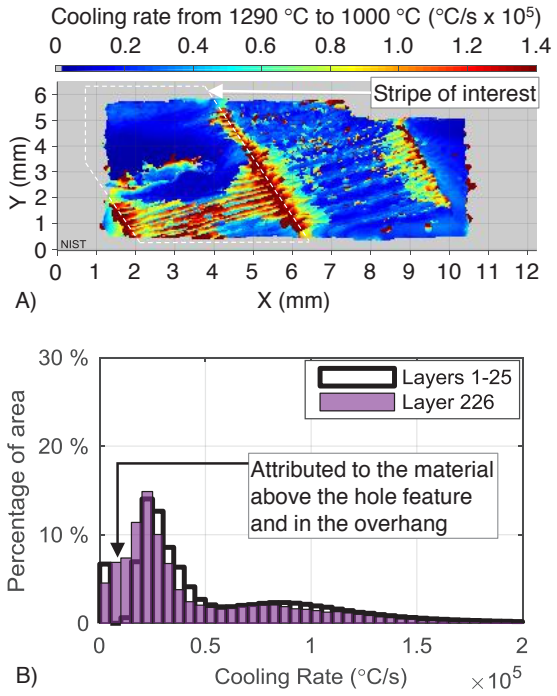


*FIGURE 10 - Cooling rate measured during Layer 226. A) Measured cooling rate at each pixel in the layer, B) comparison with Layers 1 through 25.*

to conduct heat away because it has had a chance to cool down from the prior stripe scans.

FIGURE 11 presents the cooling rates from the final layer, Layer 249. In general, the cooling rates are similar to the Layer 25, though the material at the overhang experiences a slightly slower cooling rate. However, the reduction in cooling rate at the overhang is not as drastic as above the hole (in Layer 226, FIGURE 10), likely because the overhang is 45°, whereas above the hole a much more extreme overhang is created.

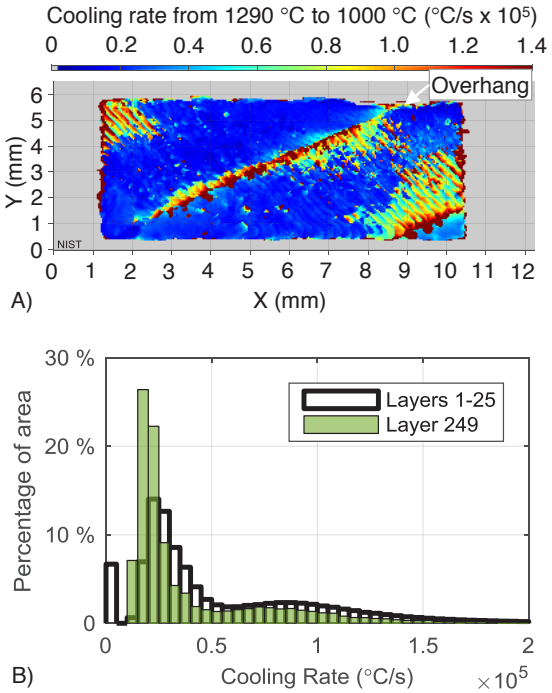


*FIGURE 11 - Cooling rate measured during Layer 249. A) Measured cooling rate at each pixel in the layer, B) comparison with Layers 1 through 25.*

## SUMMARY AND FUTURE WORK

The in situ measurements in this study reveal that the thermal processing in LPBF is extremely imprecise. Both geometry and scan strategy are shown to increase and/or decrease the cooling rates by several factors, and the interaction between the two is complex. Although improvements can be made to improve the thermal processing precision, research must first be conducted to determine the level of precision required to achieve consistent microstructure, material properties, and stresses in the part.

## REFERENCES


[1] F.-W. Goudsmit, G. Oosterhuis, E. Sluiter, and T. Peijnenburg, (2014) Typical requirements for precision mechanical parts and opportunities for additive manufacturing, *Proceedings of the ASPE Topical Meeting: Dimensional Accuracy and Surface Finish in Additive Manufacturing*, Berkeley, CA, pp. 51–55.

[2] P. Mercelis and J.-P. Kruth, (2006) Residual stresses in selective laser sintering and selective laser melting, *Rapid Prototyping Journal*, 12(5), pp. 54–265.

[3] T. Keller, G. Lindwall, S. Ghosh, L. Ma, BM. Lane, F. Zhang, U.R. Kattner, E.A. Lass, J.C. Heigel, Y. Idell, M.E. Williams, A.J. Allen, J.E. Guyer, L.E. Levine, (2018) Application of finite element, phase-field, and CALPHAD-based methods to additive manufacturing of Ni-based superalloys, *Acta Materialia*, 139, pp. 244-253.

[4] Y.M. Arısoy, L.E. Criales, T. Özel, B. Lane, S. Moylan, & A. Donmez, (2017). Influence of scan strategy and process parameters on microstructure and its optimization in additively manufactured nickel alloy 625 via laser powder bed fusion. *The International Journal of Advanced Manufacturing Technology*, 90(5-8), pp. 1393-1417.

[5] J.C. Heigel and B.M. Lane, (2018) Measurement of the melt pool length during single scan tracks in a commercial laser powder bed fusion process, *Journal of Manufacturing Science and Engineering*, 140(5).

[6] Additive Manufacturing Benchmark Test Series (AM-Bench): Class 1 benchmark test description. *https://www.nist.gov/ambench/amb2018-01-description*

[7] J.C. Heigel, and B.M. Lane, (2017) The effect of powder on cooling rate and melt pool length measurements using in situ thermographic techniques, *Proceedings of the 28th Annual International Solid Freeform Fabrication Symposium – An Additive Manufacturing Conference*, pp. 1340-1348.

[8] B. Lane and E.P. Whitenton, (2015) Calibration and Measurement Procedures for a High Magnification Thermal Camera, *NIST Interagency/Internal Report (NISTIR) – 8098.*